High-resolution photoelectron spectrometry of atomic manganese from the region of the $3p \rightarrow 3d$ giant resonance to 120 eV

S. B. Whitfield
Fritz-Haber-Institut der Max-Planck-Gesellschaft, Faradayweg 4-6, 14195 Berlin, Germany

M. O. Krause
Oak Ridge National Laboratory, Oak Ridge, Tennessee 37831-6201

P. van der Meulen
Department of Physical Chemistry, University of Amsterdam, Nieuwe Achtergracht 127, 1018 WS Amsterdam, The Netherlands

C. D. Caldwell
Department of Physics, University of Central Florida, Orlando, Florida 32816
(Received 8 February 1994)

Partial photoionization cross sections σ of the $3d$ and the $4s$ main lines and the major satellite lines following the photoionization of atomic manganese in the vicinity of the $3p \rightarrow 3d$ giant resonance are studied in detail using the constant-ionic-state technique. Previously unresolved features are seen, revealing the complex structure of this transition-metal atom. Evidence for seven excited states hidden in the giant-resonance region is uncovered. Widths of most of the observed excited states are deduced. The width of the dominant $[\mathrm{Ne}]3s^2 3p^5 3d^6 4s^2(^6P)$ state is found to be at most 1.5 eV. The origin of a pronounced dip in the partial cross section of the primary $3d$ photoionization line, which also appears in absorption, is identified. More than 15 resonance features converging to the $[\mathrm{Ne}]3s^2 3p^5 3d^5 4s^2(^7P_{4,3,2})$ limits are observed, and tentative assignments are given. In addition, nonresonant photoelectron spectra recorded from 80 to 120 eV photon energy are examined to determine the behavior of the strongest photoelectron satellite lines and very-high-lying binding energy satellites, which, until now have not been investigated.

PACS number(s): 32.80.Fb, 32.80.Dz

I. INTRODUCTION

The photoionization of atomic manganese has long been a test case for the behavior of open-shell atoms by virtue of its half-open d shell $[\mathrm{Ar}]3d^5 4s^2(^6S_{5/2})$; to date there have been numerous experimental and theoretical investigations of this system. Experimental work has primarily focused on absorption [1–6] and photoelectron spectroscopy [3,7–10] including angular resolved measurements [11–15]. On the theoretical side, both the total photoionization cross section [16–22] over various photon energy ranges and the partial photoionization cross sections of the main photoionization lines [18,22–30] have been calculated. A review of both the theoretical and experimental work up through 1991 is given by Sonntag and Zimmermann [31].

Yet, despite the extensive body of knowledge thus far accumulated, a *detailed* understanding of this system from a theoretical point of view is still lacking, even in the heavily investigated region of the $3p \rightarrow 3d$ giant resonance, where such basic quantities as the level energies of the various terms that result from the $3p \rightarrow 3d$ excitation have not been properly accounted for. Not only does theory give inconsistent results for the level energies, but even the ordering of the terms differs [16,24]. Furthermore, the dip near the maximum of the $3p \rightarrow 3d$ resonance, first seen in absorption [2], has yet to be adequately addressed by theory, where all theoretical models [16,18,24] predict only one major resonance. The situation is even worse with regard to the satellite lines associated with $3d$ and $4s$ photoionization. For example, theory has not investigated the way in which the $3p \rightarrow 3d$ resonance and other higher-lying excitations decay into the various satellite channels. At present there exist *no* theoretical calculations of satellite partial cross sections or angular distribution parameters outside the $3p \rightarrow 3d$ resonance.

Experimentally, previous measurements have lacked the resolution, both in the monochromator and in the electron spectrometer, required to elucidate the striking complexity of this open-shell system. In particular, the various autoionization resonances of the type $3p \rightarrow n\ell$, especially $3p \rightarrow 3d$, could not be resolved, and their widths and decay into satellite exit channels could not be accurately determined. In this work we present a high-resolution study of the Mn atom, concentrating on the $3p \rightarrow 3d$ resonance region and its decay characteristics into the strongest exit channels represented by the $3d$ and $4s$ photoionization lines and their major satellite lines. In so doing, we are able to reveal the presence of various excited states which all lie in the vicinity of the so-called $3p \rightarrow 3d$ giant resonance near 50 eV. In addition, we also present measurements of the relative partial cross sec-

tions of the strongest satellite lines in the region from 80 to 120 eV. Included in these measurements are some very high-binding-energy satellites. Although some of these high-binding-energy satellites have been observed previously [14], no quantitative analysis of either their binding energies or cross sections was made. These satellites gain strength above the $3p \rightarrow 3d$ giant resonance, and, in contrast to the lower-binding-energy satellites, are very weak in the region of the giant resonance. Where available, comparisons to previous measurements and calculations will be made.

II. EXPERIMENT

The experiment was conducted in two separate runs at the University of Wisconsin Synchrotron Radiation Center. The bulk of the measurements were performed on the 3-m toroidal grating monochromator (TGM), with the remainder conducted at the 6-m TGM. The details of the experimental setup have been described elsewhere [11,32]. Briefly, synchrotron radiation from the storage ring was directed through a glass capillary into a resistively heated vapor oven where a source of Mn atoms was produced by evaporation of the solid. This so-called "internal" oven, used in previous metal vapor experiments [15,33,34], serves simultaneously as the source region for the electron analyzers, i.e., the photoelectrons are created directly inside the oven. The chief advantage of this design is a reduction of the overall vapor pressure required to produce a measurable signal. The oven was typically operated at about 780 ° C, producing a vapor pressure in the oven in the lower 10^{-4} Torr. The electrons were energy analyzed in a spherical sector plate electrostatic analyzer having a resolution of 1% of the pass energy. In order to avoid the influence of any angular distributions on the measured intensities, the analyzer was set to the pseudomagic angle θ_m. We used $\theta_m = 57.8°$ during the run on the 3-m TGM and $\theta_m = 58.2°$ while on the 6-m TGM, corresponding to a polarization of 77% and 75%, respectively, as determined in separate calibrations.

Photoelectron spectra were collected in two different modes: the traditional photoelectron spectrometry (PES) mode, in which spectra are recorded at a fixed photon energy while scanning the accelerating (retarding) voltage of the source cell or the analyzer plates; and the constant-ionic-state (CIS) mode, in which spectra are recorded by simultaneously scanning the incident photon energy and the accelerating (retarding) voltage of the source cell so as to always observe electrons which correspond to the same final ionic state.

The resolution of the CIS scan depends solely on the bandpass of the monochromator. The resolution of the electron spectrometer only plays a role insofar as it must be capable of isolating single final states of the ion. For the run conducted at the 3-m TGM, where all CIS measurements were made, entrance and exit slit settings of 0.38 mm were found to be an excellent compromise between monochromator resolution and flux. The bandpass of the monochromator for these slit settings was determined from a convoluted fit of the He $2s2p$ autoionizing resonance. Using the older value of the He $2s2p$ width, $\Gamma = 0.038$ eV [35], we found the bandpass from a best fit to be 0.30(2) Å.

Changes in photon flux during the course of the CIS scan resulting from the decay of the storage ring beam current and changes in the throughput of the monochromator at different photon energies were corrected by dividing out a Ni mesh current which was simultaneously recorded during each CIS scan. Although we did not correct the Ni mesh current for the influence of second-order radiation, we expect this contribution to amount to less than 10% of the total signal. In addition, no correction to the CIS scans due to the influence of the Ni photoionization yield was made, as none was available in the energy region studied. However, comparison with Au, which should be similar to Ni in this region, indicates a change in photoionization yield of about 5% from the beginning of the CIS scan to the end [36,37]. The location of the Ni mesh was just beyond the final optics of the 3-m beamline, just before the entrance to the experimental setup. In addition, it was necessary to account for any decrease in light intensity during the CIS scan which could arise from deposition of the Mn on the light collimating capillary. This was accomplished by recording a reference PES spectrum at a conveniently chosen energy both before and after the CIS scan. After normalizing this PES scan to counting time and the storage ring beam current, any difference in intensity between the two PES scans could then be used to correct the CIS scan. This calibration also served to correct for any gradual change in the oven yield during the course of the CIS scan as well as any small shifts that may have occurred in the peak positions. Additional PES scans were recorded at the initial and final photon energies of the CIS scan to determine the background of the CIS spectrum. Following subtraction of the background and application of the correction procedures outlined above, each CIS scan then represents a measure of the relative partial cross section as a function of photon energy for the feature in question. CIS spectra took anywhere from 25 minutes up to an hour to record, depending on the strength of the satellite or main line and the initial beam current of the storage ring.

PES spectra were recorded in two different ways: the constant pass-energy mode (source scan) in which the analyzer plates are maintained at a fixed voltage and the source cell is ramped; and the constant accelerating (retarding) voltage mode (plate scan) in which the accelerating (retarding) voltage applied to the source cell is fixed and the analyzer plates are ramped. In the case of the source scan, the resolution is constant for every channel of the scan. In those cases where the ratio of the retarding (accelerating) voltage to the initial kinetic energy of the feature in question is relatively small, then the transmission of the analyzer is essentially constant. For values where this ratio is moderate to large, then lens effects will strongly affect the transmission of the analyzer. For the plate scan the resolution varies as a function of the kinetic energy of the recorded features. Ideally, the transmission of the analyzers varies as the reciprocal of the pass energy of the feature in question. As in the case of the source scan, lens effects due to high

retardation (acceleration) will alter the behavior of the analyzer's transmission.

For all PES spectra presented here complete transmission corrections have been applied, including those necessary to account for very high retardation voltages. Thus, after subtracting the background, the integrated counts under any given peak in the PES spectrum can be taken to be the relative cross section of that feature for the photon energy at which the spectrum was recorded. In addition, the kinetic energy scale of the spectra recorded in the plate-scan mode had to be corrected because the ramping voltage was capacitively coupled. This caused a slight nonlinearity of the scan. The constants of the condenser-charging curve were determined by a suitable calibration using photoionization lines of well known binding energies.

Normalization between the various PES spectra recorded at photon energies within the range of the CIS scans and between these PES and CIS spectra was accomplished as follows. The integrated intensity of the $3d(^5D)$ main line, corresponding to the ionic configuration $3d^4(^5D)4s^2(^5D)$, recorded at 50.25(3) eV, Fig. 1, was arbitrarily set to 100. Similarly, the maximum value of this line as recorded in the CIS spectrum of Fig. 2(c) at 50.25(3) eV was also set to 100. The remaining CIS spectra were then normalized so that their relative intensities at 50.25(3) eV were equal to the relative intensities of the PES results at 50.25(3) eV as listed in Table I. Next, the integrated intensity of the PES $3d(^5D)$ main line recorded at the other photon energies was set equal to the intensity of the $3d(^5D)$ main line from Fig. 2(c) at the appropriate photon energy. Then, to assure that this normalization routine was self-consistent, the integrated intensity of every PES feature with a corresponding CIS spectrum was compared with its CIS value at the photon energy where it was recorded. In nearly all cases excellent agreement between the two data sets was found, with discrepancies rarely exceeding 10%.

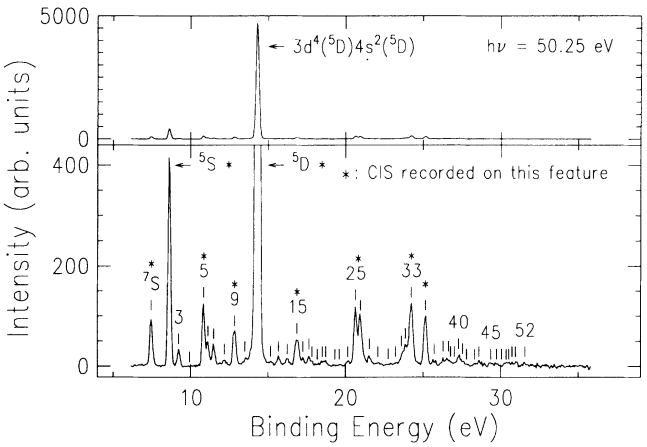

FIG. 1. High-resolution PES spectrum recorded at the pseudomagic angle at $h\nu = 50.25(3)$ eV. The upper portion shows the complete spectrum, while the lower portion, an expansion of the upper part, focuses on the satellites. The positions of the main lines and the satellites are indicated by vertical bars. An asterisk indicates that a CIS scan was recorded on that line. The spectrum consists of 512 channels with a PES resolution of 0.21(1) eV.

Integrated intensities and positions of the various PES features were found from fitting the data with multiple Pearson-7 functions [38] following background subtraction. The four-parameter Pearson-7 function can be continuously varied from a pure Lorentzian line shape to a pure Gaussian line shape, making it ideally suited to fitting Voigt profiles.

Finally, we note that although some second-order radiation was present, we chose not to use an Al filter to block it out, as most spectra showed little difference with or without the presence of the filter, and the Al filter greatly reduced the flux of the incoming radiation.

III. RESULTS AND DISCUSSION

A. High-resolution PES results

A high-resolution PES spectrum of Mn recorded in the source scan mode at $h\nu = 50.25$ eV, the maximum of the $3p \rightarrow 3d$ resonance, is shown in Fig. 1. This spectrum has been normalized in the manner discussed above including background subtraction and transmission correction. The upper panel gives an overview of the spectrum, which is dominated by the main $3d(^5D)$ photoionization line. The lower panel shows an expansion of this spectrum focusing on the two $4s$ main lines, which correspond to the $3d^5(^6S)4s(^7S,^5S)$ configurations, and the satellites of the $4s$ and $3d$ lines. The PES resolution of isolated, single configuration lines in this spectrum corresponds to a full width half maximum (FWHM) of 0.21(2) eV. The entire spectrum took 45 minutes to record with a peak-height maximum of about 18 000 counts in the main $3d(^5D)$ line prior to the normalization procedure discussed in Sec. II. Asterisks above the peak numbers indicate those features on which a CIS spectrum was recorded.

Several features are now completely or partially resolved: satellite 3, satellites 5, 6, and 7, and satellites 25 and 26. In addition, there is also very strong evidence for the existence of at least four times as many satellites as previously observed [7,8,11], although many of these are of a very weak nature. Table I gives a complete listing of the features observed in this spectrum, including binding energies, relative intensities with respect to the $3d(^5D)$ main line, peak 11, and assignments based mostly on the optical data of Corliss and Sugar [39]. We converted all wave numbers from Ref. [39] using the constant $1.239\,852\times10^{-4}$ eV cm, and determined all Mn II level energies with respect to the first ionization potential, 7.4368(1) eV, as given in that work. This differs slightly from a more recent determination [40] in which a value of 7.434 08(2) was measured. A comparison with the optically derived binding energies and previous PES experimental binding energies [8,11] is also given in Table I. The agreement between our PES results and previous PES results is excellent. The only discrepancy arises in the assignment of satellite 26. In previous PES studies

TABLE I. Binding energies of the Mn main lines and satellites and their relative intensities measured at 55.5° and $h\nu = 50.23(5)$ eV. Unless otherwise indicated, the energies are the weighted average of the various J components of the final term listed in the seventh column.

	Binding energy (eV)				Rel. Int. (%)	Assignment
Line	This work	Ref. [39]	Ref. [11]	Ref. [8]	This work	Ref. [39]
1	7.437[a]	7.437	7.437[a]	7.44	1.9(2)	$3d^5(^6S)4s(^7S_3)$
2	8.611[a]	8.611	8.611[a]	8.60(5)	7.5(7)	$3d^5(^6S)4s(^5S_2)$
3	9.23(4)	9.245	9.2(1)	9.3(1)	0.61(7)	$3d^6(^5D)$
4[b]	9.94(4)					?
5	10.86(4)	10.855	10.9(1)	10.8(1)	2.3(2)	$3d^5(^4G)4s(^5G)$
6	11.14(4)	11.140 11.146	11.2(1)	11.2(1)	0.86(9)	$3d^6(^3P_2)$ $3d^5(^4P)4s(^5P)$
7	11.51(4)	11.507	11.6(1)	11.5(1)	0.87(9)	$3d^5(^4D)4s(^5D)$
8	12.19(4)	12.224			0.30(5)	$3d^5(^6S)4p(^7P)$
9	12.85(4)	12.842	12.8(1)	12.8(1)	1.7(2)	$3d^5(^4F)4s(^5F)^c$
10	13.61(5)	13.620			0.44(5)	$3d^5(^4F)4s(^3F)$
11	14.301[a]	14.301	14.301[a]	14.20(15)	100.00	$3d^4(^5D)4s^2(^5D)$
12	15.16(5)	15.196			0.25(5)	$3d^5(^2D)4s(^3D)$
13	15.68(4)	15.704			0.46(5)	$3d^5(^4G)4p(^5F)^c$
14	16.24(4)	16.225			0.40(4)	$3d^5(^4P)4p(^3D)^c$
15[d]	16.87(4)	16.837 16.906		16.8(2)	1.5(2)	$3d^5(^4D)4p(^3P)^c$ $3d^5(^6S)5s(^5S_2)$
16	17.25(4)	17.246 17.250			0.33(5)	$3d^5(^2I)4p(^1H_5)^c$ $3d^5(^2I)4p(^1K_7)^c$
17	17.64(4)	17.622 17.632			0.41(5)	$3d^5(^6S)4d(^5D)$ $3d^5(^2F)4p(^3G)$
18	17.84(4)	17.840			0.12(5)	$3d^5(^4F)4p(^3G)^c$
19	18.18(4)	18.208 18.214			0.09(5)	$3d^5(^2H)4p(^1I_6)^c$ $3d^5(^6S)5p(^5P)$
20	18.50(4)	18.479 18.496 18.529			0.19(5)	$3d^5(^2G)4p(^1H_5)^c$ $3d^44s4p(^5P)$ $3d^5(^2F)4p(^1G_4)^c$
21	18.73(4)	18.717 18.743		18.9(3)	0.22(5)	$3d^44s4p(^5F)$ $3d^5(^2F)4p(^3G)^c$
22	19.33(4)				0.02(1)	?
23	19.60(5)	19.638 19.640 19.645			0.07(5)	$3d^5(^6S)6s(^5S_2)$ $3d^5(^6S)4f(^7F)$ $3d^5(^6S)4f(^5F)$
24	20.15(4)	20.170			0.21(5)	$3d^5(^4G)5s(^3G)$
25	20.66(4)	20.659 20.690 20.695	20.6(2)	20.6(2)	2.5(2)	$3d^44s4p(^5F)$ $3d^44s4p(^5P)$ $3d^5(^4D)5s(^5D)$
26[e]	20.98(4)	20.982	21.0(2)	20.8(2)	2.4(2)	$3d^5(^6S)6d(^7D)$
27[e]	21.55(4)	21.558			0.51(4)	$3d^5(^6S)8s(^5S_2)$
28	22.10(5)				0.21(5)	?
29	22.76(4)			22.5(3)	0.12(5)	?
30	23.23(4)				0.18(5)	?
31	23.61(5)				0.52(6)	?
32	23.87(4)				0.93(8)	?
33	24.24(4)		24.2(1)	24.2(2)	3.3(3)	$3d^44s4d^f$ $3d^4(^5D)4s5s^g$
34	25.15(4)		25.1(1)	25.1(2)	2.4(2)	$3d^44p^{2f}$ $3d^4(^5D)4s4d^g$
35	25.71(4)				0.24(5)	?
36	26.30(5)			26.3(2)	0.26(5)	?
37	26.63(5)				0.31(4)	?
38	26.76(4)				0.15(5)	?
39	27.01(4)				0.10(5)	?
40	27.27(4)		27.5(2)	27.4(2)	0.46(5)	$3d^4(^5D)4s6s^h$
41	27.54(5)				0.17(5)	$3d^4(^5D)4s5d^h$

TABLE I. *(Continued).*

Line	Binding energy (eV) This work	Ref. [39]	Ref. [11]	Ref. [8]	Rel. Int. (%) This work	Assignment Ref. [39]
42	27.79(4)				0.07(5)	?
43	28.31(4)				0.10(5)	?
44	28.59(5)		28.5(2)	28.6(2)	0.21(5)	$3d^4 4s5d^f$
45	29.35(4)			29.4(2)	0.17(5)	?
46	29.73(4)				0.12(5)	?
47[b]	30.06(5)					?
48	30.36(5)				0.15(5)	?
49	30.53(5)				0.10(5)	?
50	30.74(5)				0.09(5)	?
51	30.97(5)				0.16(5)	?
52	31.58(5)				0.14(5)	?

[a]Reference energies by which the binding energy scale was determined.
[b]This satellite, although not present in this spectrum, can be seen at other photon energies.
[c]According to Ref. [39], this configuration contains a mixture of terms. Here only the leading term is given.
[d]There are probably two peaks here as the peak width is greater than the other peaks.
[e]According to the optical data [39], there are several other nearby states which could be included in the assignment.
[f]Assignment from Ref. [11].
[g]Assignment from Ref. [8].
[h]Assignment based on our analysis. Because satellite 40 is enhanced at the $3p \rightarrow 5s$ resonances, we believe it is associated with the shakeup of the $5s$ electron to a $6s$ orbital during the decay. We observe similar enhancement of satellite 41 at the lowest $3p \rightarrow 4d$ excitation, indicating that it corresponds to the shakeup of the $4d$ electron to the $5d$ orbital during the decay.

[7,8,11] this line, unresolved from the neighboring line 25, was assigned to the $3d^4(^5D)4s4p(^5P)$ configuration with a binding energy of 20.690 eV [39]. As we are able to partially resolve line 25 from 26, we can make a much more accurate determination of its binding energy. According to the optical data, the most likely candidate is the $3d^5(^6S)6d(^7D)$ line at 20.982 eV, although other nearby optically observed states could also be possible.

Finally, a further discussion of the assignments is in order. According to the optical data of Corliss and Sugar, there are many cases in which a particular configuration was found to contain a mixture of different LS terms. The percentage composition of the various terms as determined by Corliss and Sugar was based primarily on a semiempirical method. This method treats the radial matrix elements appearing in the energy matrix as parameters which are subsequently determined via a least squares fitting procedure to the observed level [39]. When a given configuration was listed as containing a mixture of terms, we have given only the leading term (that which has the largest percentage of the total composition) in Table I. However, we have marked it by a superscript c to indicate that this configuration is a mixed-term state. One should consider even these mixed-term assignments to be no more than a rough guide to the true quantum character of a particular level.

B. CIS results: overview

In order to reveal the behavior of the main lines and their associated satellites in the region from 43 to 60 eV in greater detail, CIS spectra were recorded on all features marked with an asterisk in Fig. 1. Conversely, CIS spectra on known lines corresponding to a given ionic state also help to identify excited states of the neutral and yield their decay probabilities into the major exit channels. This photon energy region includes the giant $3p \rightarrow 3d$ resonance and Rydberg excitations of the $3p$ electron to unoccupied s and d orbitals. The results are shown in Fig. 2, with the designation of the main line or the satellite given in the upper left hand corner of the figure panels. All spectra have been normalized with respect to each other as discussed in Sec. II so that a direct comparison of their relative intensities can be made. The photon energy scale was determined by taking resonance 4, clearly visible in every spectrum, as a reference. We have used the value of 48.1 eV for its level energy, as given in Ref. [31]. The ionization limits for removal of a $3p$ electron leaving the final state of the ion in a ^7P term are also indicated. These values come from the recent measurements of Ford *et al.* [41]. Finally, we note that those features marked by an asterisk in Fig. 2 arise from a Coster-Kronig interloper which results from the filling of a $3p$ hole created by second-order radiation.

Numbers with corresponding lines in all spectra indicate the position of resonances. Table II gives the energies and suggested assignments of these resonances. For most resonance features natural widths are also given. These were determined by fitting the resonance features of interest with a Shore profile [42] including convolution with a monochromator bandpass of 0.30 Å. The Shore parametrization is similar to that of Fano [43], and a

simple correspondence between the A, B, and C parameters of the Shore profile and the q, σ_a, and σ_b parameters of the Fano profile exists [44,45]. Neither formulation accounts for interacting resonances which may lie very close to each other, or within the natural width of each other. A comparison of level energies to previous measurements and two theoretical calculations is given in Table III. Due to limited space, not all resonances indicated in Table II are marked on the figure. Where two resonances are indicated in Table II, such as 17a,b, only a single number designation is shown in the figure.

In order to obtain a reasonable counting rate during

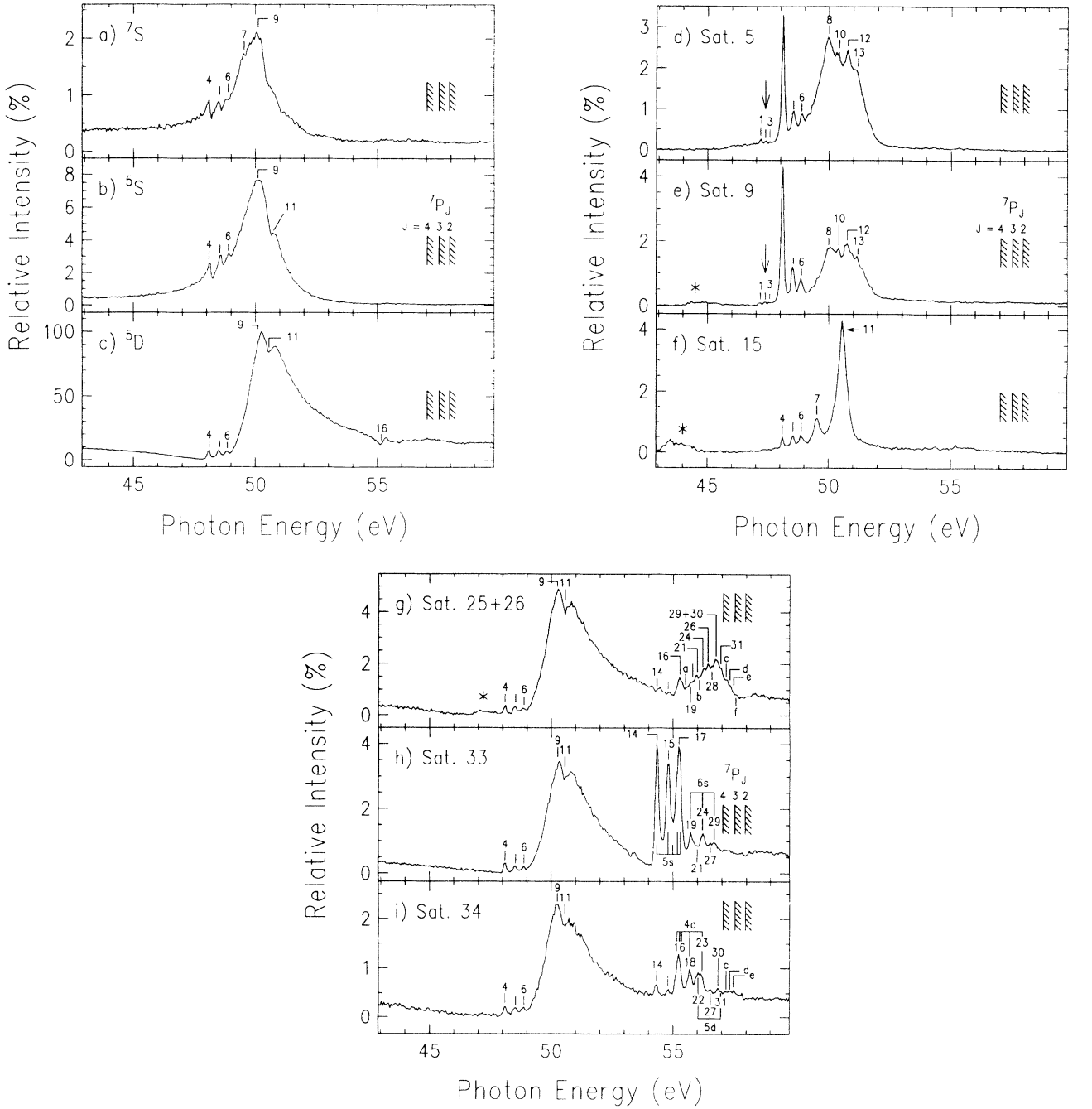

FIG. 2. CIS scans of the main lines and selected satellites recorded at the pseudomagic angle covering the region of the $3p \rightarrow n\ell$ resonances including the $3p \rightarrow 3d$ giant resonance. The ionic state designations refer to those in Fig. 1. All spectra were recorded with a monochromator bandpass of 0.30(2) Å and consist of 341 points each. The step size is 50 meV. Resonance positions are indicated by bars. All spectra have been normalized with respect to each other so that their relative intensities can be directly compared. The asterisks in the spectra indicate the position of the Coster-Kronig interloper as described in the text. The positions of the $^7P_{4,3,2}$ ionization limits are also shown. Recording times for each spectrum varied from about 30 to 60 minutes.

accumulation of these spectra, a lower PES resolution than that shown in Fig. 1 was required. With a resolution of 0.65(2) eV, it was not possible to separate satellites 25 and 26. Thus the resulting CIS spectrum, Fig. 2(g), represents a sum of both of these satellite states. The CIS scans, which are directly proportional to relative partial cross sections, can be placed on an absolute scale (megabarns) by multiplying them with a factor of 0.624. This factor was determined by normalizing the intensity of the $3d(^5D)$ main line at 50.80(3) eV, Fig. 2(c), to the value of 55.2(5.4) Mb as given by Krause, Carlson, and Fahlman [11].

CIS measurements have been made for both the $4s(^5S)$ and the $4s(^7S)$ main lines separately, and for satellites 5, 9, 25+26, and 34. Our measurements differ principally from earlier CIS measurements [8] in a superior

TABLE II. Mn I resonance energies and widths in the energy range from 47 to 58 eV, and their suggested assignments. All assignments are with respect to a $1s^22s^22p^63s^23p^5$ core.

Line	Level energy (eV)	Width (eV)	Assignment
1	47.18(3)	< 0.054	$3d^64s^2(^6F_{7/2})$
2	47.38(3)	< 0.054	$3d^64s^2(^6F_{5/2})$
3	47.56(3)	< 0.055	$3d^64s^2(^6F_{3/2})$
4	48.10[a]	0.92(6)	$3d^64s^2(^6D)$
5	48.54(3)	0.14(1)	$3d^64s^2(^4P_{5/2})$
6	48.88(3)	0.16(3)	$3d^64s^2(^4P_{3/2})$
7	49.52(3)	0.33(3)	$3d^64p^2(^{2S+1}L)$
8	50.00(3)	0.80(6)	$3d^64s^2(^{2S+1}L)$
9	50.1(1)	1.50(5)	$3d^64s^2(^6P)$
10	50.39(4)	0.35(6)	$3d^64s^2(^{2S+1}L)$
11	50.55(3)	0.48(2)	$3d^64p^2(^6P)$
12	50.75(4)	0.42(6)	$3d^64s^2(^{2S+1}L)$
13	51.15(6)	0.70(7)	$3d^64s^2(^{2S+1}L)$
14	54.34(3)	0.10(1)	$3d^54s^2(^7P_4)5s(^6P_{7/2})$
15a	54.80(3)	0.11(1)	$3d^54s^2(^7P_3)5s(^6P_{5/2})$
15b	54.99(3)	0.10(1)	$3d^54s^2(^7P_3)5s(^6P_{7/2})$
16a	55.16(4)	0.10(1)	$3d^54s^2(^7P_4)4d(^6P_J)$
16b	55.25(3)	0.10(1)	$3d^54s^2(^7P_4)4d(^6P_J)$
16c	55.28(3)		$3d^54s^2(^7P_4)4d(^6P_J)$
16d	55.35(4)		$3d^54s^2(^7P_4)4d(^6P_J)$
17a	55.18(4)	0.10(1)	$3d^54s^2(^7P_2)5s(^6P_{5/2})$
17b	55.29(4)	0.10(1)	$3d^54s^2(^7P_2)5s(^6P_{7/2})$
a	55.50(5)		?
18	55.68(3)	0.10(1)	$3d^54s^2(^7P_3)4d(^6P_J)$
19	55.72(3)	0.10(1)	$3d^54s^2(^7P_2)6s(^6P_{7/2})$
20	55.89(5)		?
21	55.99(4)	0.10(1)	$3d^54s^2(^7P_4)5d(^6P_J)$
22	56.03(3)	0.10(1)	$3d^54s^2(^7P_4)5d(^6P_J)$
b	56.07(4)		$3d^54s^2(^7P_4)5d(^6P_J)$ $3d^54s^2(^7P_2)4d(^6P_J)$
23	56.19(4)	0.10(1)	$3d^54s^2(^7P_2)4d(^6P_J)$
24	56.21(3)	0.12(1)	$3d^54s^2(^7P_3)6s(^6P_J)$
25	56.37(5)		?
26	56.42(3)		$3d^54s^2(^7P_4)6d(^6P_J)$[c]
27	56.52(4)	0.11(1)	$3d^54s^2(^7P_3)5d(^6P_J)$
28	56.58(4)		?
29	56.69(4)	0.12(1)	$3d^54s^2(^7P_2)6s(^6P_J)$
30	56.84(3)	0.11(1)	$3d^54s^2(^7P_2)5d(^6P_J)$
31	56.95(5)		$3d^54s^2(^7P_2)5d(^6P_J)$
Limit	57.04(3)[b]		$3d^54s^2(^7P_4)$
c	57.17(4)		?
d	57.32(5)		$3d^54s^2(^7P_2)6d(^6P_J)$[c]
e	57.47(5)		?
Limit	57.53(3)[b]		$3d^54s^2(^7P_3)$
f	55.57(4)		?
Limit	57.96(3)[b]		$3d^54s^2(^7P_2)$

[a]Reference photon energy taken from Ref. [31].
[b]Reference [41].
[c]Assignment is based on a quantum-defect analysis.

TABLE III. Comparison of Mn I resonance energies (in eV) with previous measurements and calculations. The first seven absorption values are from Ref. [2], while the remaining values are taken from Ref. [5]. The last three absorption level energies given here agree within 10 meV with the later work of Ref. [6], except for resonance 14, where a level energy of 54.50 eV is given.

	Experiment			Theory	
Line	This work	Absorp.	Ref. [8]	Ref. [16]	Ref. [24]
1	47.18(3)	47.144(9)		47.09	
2	47.38(3)	47.346(11)		47.30	
3	47.56(3)	47.49(2)		47.45	
4	48.10[a]	48.074	48.2(1)	48.44	47.427[b]
5	48.54(3)	48.501(4)		48.89	46.050
6	48.88(3)	48.832(9)		49.17	46.293
9	50.1(1)	50.40(5)	50.1(1)	51.14[c]	50.413[c]
11	50.55(3)		50.60(5)		
13	51.15(6)		51.1(1)		
14	54.34(3)	54.38	54.4(2)		
15a	54.80(3)	54.84	54.9(2)		
17a	55.18(4)	55.35	55.3(2)		
17b	55.29(4)				

[a]Reference photon energy taken from Ref. [31].
[b]This value is the J-weighted average of the $^6D_{7/2}$ and the $^6D_{3/2}$ terms. The energy of the $^6D_{5/2}$ term is 45.221 eV.
[c]This value is the J-weighted average of the $^6P_{7/2}$, $^6P_{5/2}$, and $^6P_{3/2}$ terms.

resolution, namely, 0.30 Å versus 0.89 Å, revealing resonances which have not been previously seen in emission, although they are clearly evident in absorption [2]. These are the first three resonances marked by the arrow in the spectra of satellites 5 and 9, Figs. 2(d) and 2(e). More significantly, our CIS spectra of the satellite states also give evidence of formerly unseen excited states in the region of the $3p \rightarrow 3d$ resonance, indicating that as many as seven distinct resonances could be present. In addition, this improved resolution, particularly in the region of the $3p \rightarrow ns, nd$ Rydberg excitations (where $n \geq 5$ for s electrons and $n \geq 4$ for d electrons), allows us to determine not only the level energies for the lower-lying Rydberg excitations, but their natural widths as well.

In Fig. 3 we show a comparison of a sum of our normalized CIS results to the absorption spectrum of Meyer *et al.* [3] recorded with a resolution practically equal to ours, 65 meV at 51.0 eV, and adjusted to our CIS sum at 50.8 eV. The overall agreement between the two curves is rather good, especially as regards the shape, width, and strength of the resonance features. The largest discrepancies appear in the region of the cross section minimum, near 48.0 eV, and at the higher photon energies starting around 54 eV. We attribute these discrepancies primarily to satellite channels which have not been included in our CIS sum. For example, at $h\nu = 48.1$ eV (resonance 4), the integrated intensity of the satellites and main lines which form this CIS sum amounts to only about 73% of the total PES spectrum recorded at this resonance. At higher-lying Rydberg excitations, the population of higher-binding-energy satellites by shakeup processes becomes important [33]. Such satellites are absent from our CIS sum, as is the contribution of the $3p$ photoionization lines. This contribution, which becomes possible above 57.0 eV, is estimated to amount to about 20% of our CIS sum. Furthermore, our CIS sum does not include contributions from the double ionization of Mn which begins at $h\nu = 23.077$ eV [39]. Although normalization of the absorption data to the CIS sum at 50.8 eV automatically includes the contribution of double ionization at this energy, the CIS sum will not correctly account for the steady change in the double-ionization yield from lower to higher photon energies. Finally, we note that the slight discrepancies between the resonance positions starting around 54.0 eV are mostly due to inaccuracies in the digitization of the total absorption cross section, as can be seen from the comparison given in Table III.

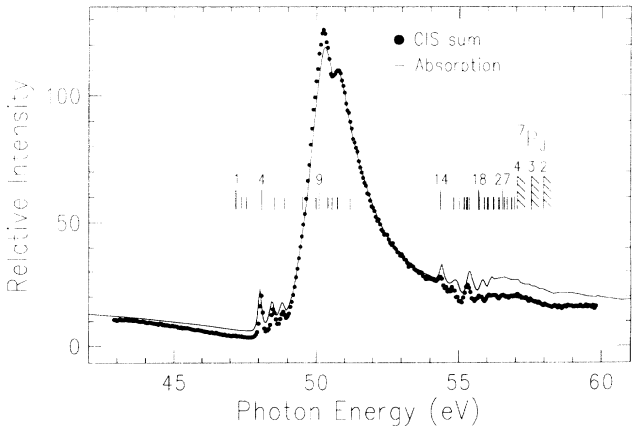

FIG. 3. Comparison between our CIS sum spectrum comprising the spectra of Fig. 2, filled circles, and the absorption spectrum of Ref. [3], solid line. The absorption spectrum was normalized to our CIS sum at 50.8 eV. Resonance positions and the $^7P_{4,3,2}$ ionization limits are also indicated.

C. CIS results: the $3p \rightarrow 3d$ giant-resonance region

Previous measurements [3,7,8,11,12] near the maximum of the $3p \rightarrow 3d$ resonance region, around 50 eV, have indicated the presence of at most three distinct excited states, including the dominant $3p \rightarrow 3d(^6P)$ excitation. Our work now demonstrates by way of CIS recordings of the various ionic states, especially the satellite states, that this region is comprised of many excited states. We determined the positions of these resonances in several ways. Resonances 1–6 are clearly resolved from each other in all spectra in which they appear, and their energies can be immediately determined from the positions of their maxima. This is also true for resonances 7 and 11 in the case of satellite 15, Fig. 2(f). Because they are well separated, it was particularly easy to fit them in order to establish their natural widths. Positions determined from the fit and from the peak maximum agreed very well with each other, as should be the case for nearly Lorentzian line shapes.

For the remaining resonances, features 8, 9, 10, 12, and 13, establishment of the resonance widths and positions required a more elaborate analysis. First, we fitted those resonances which appear in the CIS spectra of satellites 5 and 9, Figs. 2(d) and 2(e), to extract both positions and widths. Then we took the results of the fitted values of these positions and widths and held them constant while we fitted the remaining CIS spectra, Figs. 2(a)–2(c) and 2(g)–2(i), to determine the width and position of resonance 9. At this point in the analysis, it was conceivable that resonances 8 and 9 could be one and the same. However, it was not possible to obtain a consistent width or position for resonance 9 between the various fits of the CIS spectra [especially for the main lines of Figs. 2(a), 2(b), and 2(c)] by setting it equal to resonance 8. In addition, with the widths of resonances 12 and 13 fixed, as determined from the fit of satellites 5 and 9, it was completely impossible to account for the very strong asymmetry of the $3d(^5D)$ main line and satellites 25+26, 33, and 34 near 50 eV, Figs. 2(g), 2(h), and 2(i), respectively. Of course, one might expect the Shore, or Fano, parameters to change, even dramatically, but not the widths or positions of the resonances, which must remain the same regardless of what exit channel they are observed in. This led us to conclude that resonances 8, 10, 12, and 13 probably decay *only* into satellites 5 and 9 and that resonance 9 corresponds to the giant resonance which is distinct from resonance 8 and is weak or absent in the CIS spectra of satellites 5, 9, and 15.

Having made this conclusion, we could then turn to the profiles of the main lines alone [Figs. 2(a)–2(c)] to determine the width and position of resonance 9. Two aspects of the spectra of the $3d(^5D)$ and $4s(^5S)$ main lines are of particular interest: the dip giving the appearance of two peaks in the former, and the shoulder to higher photon energy in the latter. This shoulder, though much weaker, is also apparent in the $4s(^7S)$ spectrum. The shoulder of the $4s(^{5,7}S)$ main lines has not been previously observed. However, the dip in the $3d(^5D)$ main line has been seen in all the absorption spectra of Mn since the measurements of Bruhn *et al.* [2] and in the previous CIS spectra of Schmidt *et al.* [8]. Theory has not been able to accurately reproduce or explain this shape. To emphasize this point, we show in Fig. 4 a comparison of the CIS result for the $3d(^5D)$ line (filled circles) with the Hartree-Fock multiplet theory (HFMT) calculation of Davis and Feldkamp [16] (dotted line) and two versions of the many-body perturbation theory (MBPT) calculation of Garvin *et al.* [24], the coupled equation method (dashed line), and the interacting resonance method (solid line). The resonance structure beginning around 54 eV in the MBPT calculations, which corresponds to excitations of a $3p$ electron to unoccupied ns and nd orbitals, has been removed for the sake of clarity. The relativistic random-phase approximation with exchange (RPAE) calculation without renormalization, Amusia *et al.* [18], is nearly identical to the MBPT coupled equation calculation [24]. For a comparison of these theoretical results to other experimental data see Refs. [8,11,24,31].

A close examination of the $3d(^5D)$ main line indicates that the minimum of this dip corresponds very closely to the position of resonance 11 in the spectrum of satellite 15, Fig. 2(f). This is particularly apparent when the two spectra are superposed, and strongly suggests that the dip and resonance 11 are connected. Guided by this fact, we then fit the partial cross section of the three main lines, Figs. 2(a)–2(c), including convolution with the monochromator bandpass, to six Shore profiles: three accounting for resonances 4–6, and then one each for resonances 7, 9, and 11 with the widths and positions of resonances 7 and 11 *fixed* as determined from the fit of the spectrum of satellite 15. As both resonances 7 and 11 appear together in the spectrum of satellite 15, we could not reasonably exclude them from the fit of these lines. Furthermore, the shape of the $4s(^7S)$ line on the lower photon energy side suggests the presence of resonance 7.

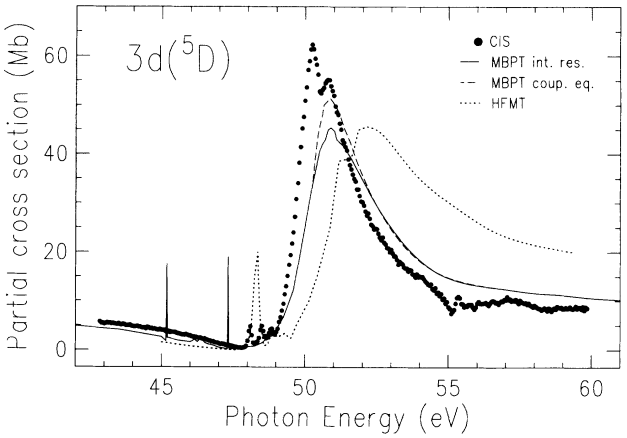

FIG. 4. Comparison between our CIS spectrum of the $3d(^5D)$ main line partial cross section, filled circles, with theory. The solid line is the MBPT calculation of Ref. [24] using the interacting resonance method, while the dashed line is their MBPT calculation using the coupled equation method. The dotted line is the HFMT calculation from Ref. [16]. The CIS result has been placed on an absolute scale using the factor of 0.624 as discussed in the text (Sec. III B).

Resonances 8, 10, 12, and 13 are not included in the fit as we have determined that they only decay into satellites 5 and 9, as discussed above.

The results are shown in Fig. 5, including the decomposition of the fit into its constituent components. The solid lines indicate the overall convoluted fit, and resonances 7 and 11, while the dashed lines indicate the remaining components. All constituent components have been plotted on top of the noninteracting continuum, the C parameter, which has been assumed to be linear in form. Not only do we obtain a nearly perfect fit of the data, at least for the $4s(^5S)$ and the $3d(^5D)$ lines, but we also obtain a totally consistent width for resonance 9, which varies by less than 10 meV from one fit to the next. This strongly suggests that the detailed structure of the Mn main lines results from the presence of resonances 7 and 11. A close inspection of Figs. 5(b) and 5(c) indicates that the profile of resonance 11 has a minimum which is *negative*. This cannot be physically possible if the dip-shoulder is to be interpreted as a simple superposition of two resonances. In such an instance, the superposition of any resonance profile with the noninteracting part of the continuum must always be *non-negative* [46–48]. However, if the two resonances are regarded as interacting, then it is only necessary that their "sum" with each other and the noninteracting part of the continuum be non-negative [49], as demonstrated in Fig. 5. Hence it appears that the formation of the dip in the $3d(^5D)$ main line and the high-energy shoulders of the $4s(^{7,5}S)$ main lines results from an interaction of resonance 11 with resonance 9 in which resonance 11 "steals" intensity from the main line and distributes it elsewhere. This depletion of intensity then appears as a negative contribution to the spectrum of the main line. We note, however, that any Shore or Fano profile does not allow for the possibility of the interaction of two nearly energetically degenerate resonances. This is only possible within a much more sophisticated theoretical treatment [50,51] in which simple parametrized formulas do not normally exist. Thus the normal definitions of the Fano and Shore parameters used in the fit in terms of interacting matrix elements lose their meaning. Nevertheless, based on the above results we believe that our conclusions are at least correct on a qualitative level. This interpretation is in contrast to that put forward previously [8] where all satellite and main line profiles in the vicinity of the giant resonance were accounted for by either the superposition of a Fano profile and a Lorentzian or two Lorentzians. In view of our higher-resolution spectra, it is simply not possible to obtain a consistent width for resonance 9 by assuming that the main lines are composed of a superposition of a Fano profile and a single Lorentzian. In addition, fits to our data under such an assumption lead to much poorer agreement with the experimental data than does the present parametrization.

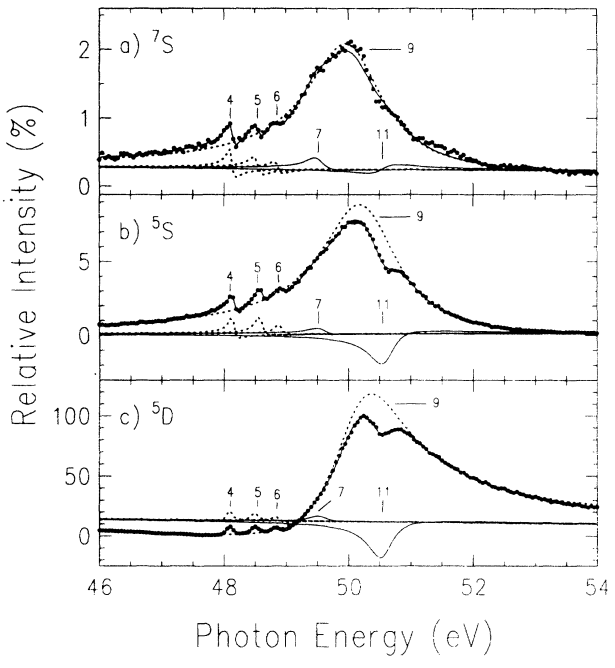

FIG. 5. Shore fits of the $4s(^{5,7}S)$ and the $3d(^5D)$ photoionization lines, including convolution with the monochromator bandpass, showing the contributions from resonances 4, 5, 6, 7, 9, and 11. The designation of the photoionization lines is given in the upper left hand corner of the figure panels. Filled circles are the experimental CIS results. The solid line is the total convoluted fit, which is nearly indistinguishable from the data in panels (b) and (c), and the components of the fit corresponding to resonances 7 and 11. The decomposition of the fit into its remaining components is given by the dotted lines. All resonances are indicated by their numeric designation as given in Table II.

A type of resonance interaction similar to that described above was recently examined [28] in the case of $4s$ photoionization in Mn^+, $3d^54s(^7S)$. The partial cross section of the $4s$ line in the region of the $3p \rightarrow 3d$ resonance displayed a unique four peak structure. The first three peaks involve excitation of the $3p$ electron into the $3p^53d^54s^2(^7P_{4,3,2})$ spin-orbit split excited states which subsequently autoionize into the the $4s \rightarrow \varepsilon_p$ continuum. The fourth peak, however, is formed by interaction between the $3p \rightarrow 4s(^7P_2)$ excitation and the $3p \rightarrow 3d$ excitation in which the top of the $3p \rightarrow 3d$ excitation is "eaten away" by the interacting $3p \rightarrow 4s(^7P_2)$ resonance. This result suggests that our present interpretation for the shape of the main lines, in particular the $3d$ dip, is quite realistic. Unlike the photoionization of the $4s$ electron in Mn^+, however, the present interaction cannot be between a $4s$ and a $3d$ excited state, as the lowest-lying excitation of a $3p$ electron to the $4s$ orbital lies 3.8 eV above the location of resonance 11, see Table II. A possible origin for this resonance, no. 11, will be discussed below.

Definitive assignments for the various terms arising from the $3p^53d^64s^2$ excited-state configuration are only possible for the first six resonances and resonance 9. For the first six resonances a direct correspondence to the HFMT calculations of Davis and Feldkamp [16] can be made. Such an assignment had already been given in the absorption work of Bruhn *et al.* [2] and adopted in the PES work of Schmidt *et al.* [8]. As can be seen from Table III, there is rather good agreement between the en-

ergies of the HFMT and experiment. Furthermore, the strength and appearance of these lines as calculated by HFMT agree reasonably well with experiment, supporting the designations given here and earlier. This agreement, however, does not extend to the MBPT of Garvin *et al.* [24]. Not only do the energies of the terms differ substantially from experiment and the HFMT results, see Table III, but even the ordering of the terms is different. In the RPAE calculations of Amusia *et al.* [18] no attempt was made to incorporate this low-lying resonance structure.

According to the theoretical models [16,24,18] the $3p \rightarrow 3d(^6P_{7/2,5/2,3/2})$ excitations should be the strongest, and in strict LS coupling, the only allowed transitions from the $^6S_{5/2}$ ground state. Furthermore, according to theory, this resonance should be strongly asymmetric in the $3d(^5D)$ channel. This asymmetry is due to the interaction of the $3p \rightarrow 3d$ resonance with the underlying continua, i.e., we have autoionization where the excited $3p^5 3d^6 4s^2(^6P)$ state can decay directly into the $3p^6 3d^4 4s^2(^5D)\varepsilon p, f(^6P)$ continua. The strength and width of this resonance is a consequence of the fact that the decay is essentially a super Coster-Kronig transition where all the initial and final holes have the same principal quantum number. Although strongly asymmetric in the $3d(^5D)$ channel, theory predicts a strong but considerably weaker interaction of this excited state with the $4s$ main lines leading to a slightly asymmetric line shape in these channels. All of these qualitative predictions are satisfied by the behavior of resonance 9, and for these reasons we can confidently assign it to the $3p^5 3d^6 4s^2(^6P_{7/2,5/2,3/2})$ configuration of the excited neutral. This interpretation is also in accord with that of Schmidt *et al.* [8], who assigned the corresponding peak in their spectra to the ^6P term. As for the width of this resonance, our fit yields 1.50(5) eV, while Schmidt *et al.* found 1.34(10) eV from a fit of this resonance in the main $3d(^5D)$ channel. The discrepancy between our value and that of Schmidt *et al.* stems from the fact that they used a superposition of a Fano profile and a Lorentzian to account for the observed structure in the partial cross section of the $3d(^5D)$ line, as discussed previously. As we included no such superposition in our fit, we naturally obtained a larger natural width. Our value and that of Schmidt *et al.*, however, do not account for the spin-orbit splitting of this resonance. Although we see no apparent evidence for this splitting, its presence could imply a smaller value for the natural width than that stated above, depending on its size. According to the HFMT results [16], the total splitting is on the order of 0.3 eV, while MBPT [24] gives about 0.4 eV. Based on our results and these values, the actual natural width of a fine-structure component of this resonance could then be as low as about 1 eV. As a result, even the renormalized RPAE width of Amusia *et al.* [18], 1.40 eV, would be too large. All other natural widths are clearly too large: 2.00 eV, RPAE without renormalization [18]; 2.33 eV, MBPT [24] (average of the widths of the different fine-structure components); and 3.28 eV, HFMT [16].

For the remaining resonances in this region, 7, 8, 10–13, no definitive assignments are possible. According to both the MBPT and the HFMT calculations, there are several other possible terms of the $3p^5 3d^6 4s^2$ configuration which could be candidates. In the earlier CIS measurements of Schmidt *et al.* [8] the resonance structure observed at about 51.0 eV, corresponding to a Lorentzian in their fits, was assigned to the $3p^5 3d^6 4s^2(^4F)$ excited state as suggested by the MBPT calculations. However, as there is a significant discrepancy between the MBPT and HFMT calculations as to the energies and ordering of these terms, we have chosen not to attempt any assignments of these states, except for resonances 7 and 11 to be discussed below. We note, as in the case of resonance 9, that the widths of these resonances may in fact be less than that stated in Table II due to spin-orbit splitting.

Before we move on to consider the behavior of the lines at the higher-lying resonances, no. 14 and above, several points should be noted with regard to the behavior of the main and satellite lines in the $3p \rightarrow 3d$ resonance region. All CIS spectra show a substantial enhancement in this energy region. However, the degree of this enhancement varies considerably. The profiles of these spectra can be classified into four groups based on their common appearance as follows: (1) the $3d(^5D)$ main line and satellites 25+26, 33 and 34; (2) the two $4s(^{5,7}S)$ main lines, (3) satellites 5 and 9; and (4) satellite 15.

The profiles of group 1 all show a pronounced asymmetry, indicating strong interference between the indirect autoionization channel and the direct photoionization channel. This behavior has already been discussed with regard to the main $3d(^5D)$ photoionization line. We note that this asymmetry is only seen in those satellites which have a non-negligible off resonance intensity. We could have deduced this fact from their profiles alone. If there is any interference at all between the indirect and the direct channels for the production of these lines, then by necessity, there must be non-negligible intensity in the direct photoionization channel. Furthermore, we can also argue that the dominant LS term of these lines following coupling with the continuum electron must be a ^6P. This is required in order to satisfy the selection rules for autoionization in LS coupling, namely, that the excited state can only decay to a continuum state which has the same parity and the same final term.

The profiles of group 2 are similar to those of group 1 except that they are nearly symmetric, with a slight asymmetry towards lower photon energy. This is an indication that there is less interference between the direct and the indirect channels for production of these final states, with the primary strength of these lines arising from the decay of the excited state. This behavior was predicted by theory as discussed above. Of recent theoretical interest [27] was the strikingly nonstatistical behavior of the cross section of these lines in the vicinity of the $3p \rightarrow 3d$ resonance, as first pointed out by Krause *et al.* [11]. As shown in Ref. [27], this behavior results from unequal population of the $4s(^{7,5}S)$ main lines by the decay of resonance 9, the $3p^5 3d^6 4s^2(^6P)$ excited state. Of particular interest in our case is the effect of resonances other than 9 on the behavior of this ratio, which has not been taken into account by theory. The ratio of these lines, ^7S:^5S, covering the photon energy range from 43

to 53 eV is shown in Fig. 6. Vertical bars indicate the positions of the resonances which affect the profiles of the $4s(^7S)$ and $4s(^5S)$ lines, Figs. 2(a) and 2(b), respectively. The filled circles are the PES measurements of Krause *et al.* [11], the open circles the PES measurements of Meyer and Sonntag as cited in Ref. [27], and the dotted line the spin-polarized RPAE calculation of Amusia *et al.* [27]. As can be seen from the figure, the effect of resonances 4–6 on the overall behavior of this ratio is quite small. There is rather good agreement between our CIS results, the earlier PES data, and theory. Discrepancies between 52 and 54 eV could result from an inadequate background subtraction due to very low signal just outside the main $3p \rightarrow 3d$ resonance and the influence of satellite 3 on the $4s(^5S)$ partial cross section in the different measurements. The very low signal in this region, see Figs. 2(a) and 2(b), is also reflected in the rather large uncertainty ascribed to the CIS ratio near 54 eV. We note that excellent agreement between theory and experiment continues up to about 65 eV [27]. However, at higher photon energies the experimental values of this ratio deviate significantly from those predicted by theory. For example, Meyer and Sonntag (see Ref. [27]) find a ratio of 5.2(4) at 80 eV compared to a theoretical value of 3.0, and we measure a ratio of 4.5(6) at 90 eV while theory [27] predicts a value of about 2.3.

The profiles of group 3 show a marked deviation from both groups 1 and 2. They reveal structure which is not visible in the other lines and appear to be quite symmetric. That these lines are so symmetric indicates little interference between the direct and indirect paths leading to the final state of the ion, with the satellites having very little strength outside of this resonance region. Perhaps the most interesting feature, however, is the overall width of these satellites, which is considerably smaller than that displayed by either group 1 or group 2. For resonances 8, 10, 12, and 13, this can be understood qualitatively as follows. According to our assignments, the

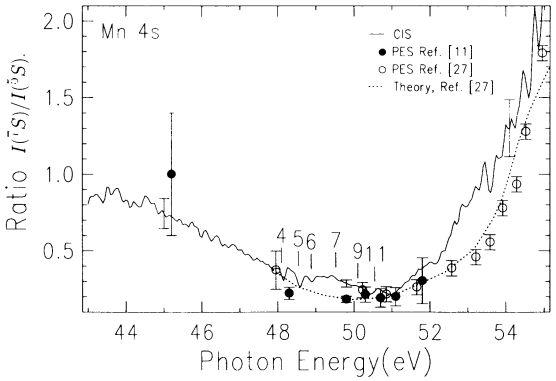

FIG. 6. CIS intensity ratio of the $4s(^7S)$:$4s(^5S)$ lines in the vicinity of the $3p \rightarrow 3d$ resonance region, solid line. Resonance positions are indicated by vertical bars along with their numerical designation from Table II. The filled circles are the PES results from Ref. [11], the open circles the PES values of Meyer and Sonntag as given in Ref. [27], and the dotted line the theoretical result of Ref. [27]. The CIS ratio has been smoothed once.

higher-lying terms of the $3p^5 3d^6 4s^2$ configuration involve terms other than the ^6P. Additional possibilities are [16] ^2D,^2F; ^4D,^4F,^4G,^4H, and ^4I. If we assume that these terms accurately represent the dominant LS component of these excited states, then upon decay they must populate states of the ion whose total term, including coupling with the outgoing continuum electron, is the same as in the excited state. This implies that no ^6P terms of the continuum state can be populated. According to the calculations of Davis and Feldkamp, transitions from excited states with ^6D and ^6F terms were substantially weaker than those from ^6P states. In fact, the widths of the transitions from ^6D excited states were found to be identically zero and those from ^6F to be about 40 meV. Only after inclusion of the spin-orbit interaction, which then mixed the ^6P, ^6D, and ^6F excited states having the same value of the total angular momentum J, did the widths of the ^6D and ^6F states become comparable to experimental values. Similar conclusions were also reached in the MBPT calculation of Garvin *et al.* [24]. Although the exact configurations of the excited states in question here are not the same as those explicitly calculated by Davis and Feldkamp, it is likely that their natural widths will also be less than that for the ^6P states because they involve decay of configurations with terms other than the ^6P.

The profile of group 4, comprising only satellite 15, is unique. Its peculiar appearance was first noted in the previous CIS measurements of Schmidt *et al.* [8]. As in the group 3 case, the strong Lorentzian profile of this line indicates that there is little or no interference between the direct and indirect channels for the production of this satellite. Furthermore, it is clear from Fig. 2(f) that outside the giant-resonance region this line is practically nonexistent. According to the level energies of Corliss and Sugar [39] there are two possible candidates for this line: $3d^5(^4D)4p(^3P)$ and $3d^5(^6S)5s(^5S)$. As regards the latter designation, one would expect this state to be strongly populated at the $3p^5 3d^6 4s^2(^6P)$ resonances as it differs from the $3d^5(^6S)4s(^5S)$ line in that a $4s$ electron has been shaken up to a $5s$ level. Hence, if one disregards the small energy difference in the outgoing continuum electron, then this transition should differ only by the square of an overlap matrix element, $\langle 4s|5s\rangle$, from that to the $3d^5(^6S)4s(^5S)$ state. Although this transition could be considerably weaker due to the overlap matrix element, it should have a similar profile. However, we see nothing in common in the profile of this satellite and the $4s(^5S)$ main line, suggesting that this cannot be the correct designation. This leaves only the alternative configuration. We note that Schmidt *et al.* [8] ruled out the $3d^5 4p$ final ionic state designation because they expected that other nearby satellites which have the same configuration but different final terms, see Table I, should behave in a similar manner. Because they saw no evidence of similar behavior in these other satellites, they concluded that this state was most likely described by a $3d^5(^6S)5s(^5S)$ configuration.

A simple inspection indicates that it is not possible to populate the $3d^5(^4D)4p(^3P)$ satellite from an excited state of the type $3p^5 3d^6 4s^2$, as this would require a con-

jugate shakeup of the $4s$ electron during the autoionizing decay. However, this satellite could be populated by a $3p^5 3d^6 4p^2(^6P)$ excited state which arises from configuration interaction with the main $3p^5 3d^6 4s^2(^6P)$ excited state. According to Ref. [12] the only appreciable configuration interaction in the ground state, 5%, was that resulting from the $3p^6 3d^5 4p^2(^6S)$ configuration. Hence it is likely that mixing between the primary $3p^5 3d^6 4s^2(^6P)$ and secondary $3p^5 3d^6 4p^2(^6P)$ excited-state configurations is also significant. The presence of this additional configuration would then explain why satellite 15 appears so different from the others, because it would be fed only by that portion of the mixed excited state involving the $4p^2$ configuration. Although this additional configuration cannot populate the main lines for the same reason that the primary configuration cannot populate satellite 15, it is only necessary that it interact significantly with the primary excited-state configuration in order to affect the main line partial cross sections. Then, the main line partial cross sections would simply map out this interaction in the excited state which populates them, as suggested by the dip in Fig. 5. Perhaps it should not seem so surprising that such an interaction could take place when one considers that resonance 11 is literally embedded in resonance 9. A further strengthening of this interaction is likely because each configuration has the same symmetry. The presence of such an excited state would also explain why theory has failed to accurately reproduce the dip in the $3d(^5D)$ main line partial cross section, because the specific configuration interaction suggested here was not taken into account. However, even this interpretation may not be correct. For example, resonances 4–6 should not be able to populate this satellite if one assumes the $3d^5(^4D)4p(^3P)$ designation is correct. The appearance of these resonances could result from the population of an overlapping satellite. According to Table I, satellite 15 is probably composed of two features. At the lower spectrometer resolution at which the CIS scan of this satellite was recorded, the presence of an overlapping satellite could not have been excluded. Furthermore, in strict LS coupling population of a ^3P state by a ^6P state is spin forbidden because the continuum electron cannot couple to a triplet state to form a sextet state. Hence a clear understanding of the observed behavior will have to await a thorough theoretical treatment.

D. CIS results: the $3p \rightarrow ns, d$ Rydberg excitations

With the exception of resonance 16, which is clearly evident in the CIS spectrum of the $3d(^5D)$ main line, the higher-lying resonances, those above 13, are only visible in the spectra of satellites 25+26, 33, and 34. According to Table I these satellites are mainly associated with the shakeup of a $3d$ or $4s$ electron following photoionization. Level energies of the resonances were primarily determined from the loci of the peak maxima. Superposing the spectra allowed us to distinguish between very closely lying resonances which would often occur in only one or two of the spectra, but not in all three. Extremely weak resonances, and those which appear in only one or two of these satellite spectra or those whose existence could be arguably questioned, have been designated by a single roman letter. For the resonances that are plainly evident, 14, 15, 17, 19, 24, and 29 in the spectrum of satellite 33 [Fig. 2(h)], and 14, 15, 16, 18, 22, 23, 27, and 30 in the spectrum of satellite 34 [Fig. 2(i)], fits were made to determine both their level energies and their natural widths. In contrast to the resonances associated with the $3p \rightarrow 3d$ excitation, nos. 1–13, nearly all the Rydberg levels have the same width, on the order of 0.1 eV. Except for resonances 1–4, these widths are substantially smaller than those involving the $3p \rightarrow 3d$ transitions. Qualitatively this would be expected as the decay of the Rydberg states does not involve a super Coster-Kronig transition. Careful scrutiny of lines 15 and 17 of satellite 33 indicate that there is another resonance lying between 15 and 17, and that 17 is, in fact, composed of two lines. These lines have been designated as 15b and 17b in Table II although they have not been labeled in the figure. As discussed below, these features are likely to be states with different final J values of the same configuration. Furthermore, small shifts in the position of resonance 16 between the spectra of satellites 25+26 and 34, Figs. 2(g) and 2(i), indicate that this resonance is composed of at least four lines, all of which are probably different final J values of the same configuration.

The energy spacings of resonances 14, 15, and 17, see Fig. 2(h), come very close to the energy spacings of the fine-structure limits of the $3p^5 3d^5 4s^2(^7P)$ configuration as measured by Ford *et al.* [41]. This suggests that these lines originate from the decay of excited states which have the same configuration and term, but with differing fine structure. These lines almost certainly result from the decay of the $3p^5 3d^5 4s^2 5s(^6P)$ excited state which one would intuitively expect to require a lower excitation energy than that to the $3p^5 3d^5 4s^2 4d(^6P)$ state. This expectation is borne out in the MBPT calculations of Garvin *et al.* [24] where the lowest-lying Rydberg excitations are to a $5s$ orbital followed by those to the $4d$ orbital. This interpretation is also in agreement with Schmidt *et al.* [8], where these resonances were first observed in emission. The strengths of these resonances in satellite 33 strongly suggest that this line be assigned to the $3d^4(^5D)4s5s$ configuration and not the $3d^4 4s4d$ configuration, see Table I. The former can be directly populated via a type of spectator transition of the $3p^5 3d^5 4s^2 5s$ configuration, while the latter cannot, since it would require the $5s$ electron to shake up into the $4d$ level. In the shake picture this type of transition would not be allowed because of the orthogonality between the angular parts of the $5s$ and $4d$ wave functions.

As discussed briefly above, the CIS spectrum of satellite 33 strongly suggests that an additional feature lies between resonances 15 and 17, and that resonance 17 is composed of two features. This is in contrast to resonance 14, which appears to be an isolated line. To see how this might be possible, consider the following coupling scheme for these excitations. First, since we begin from a $^6S_{5/2}$ ground state, the final total angular momentum J of the excited state can only be 7/2, 5/2, or

3/2. Next, let us presume that all the electrons in the configuration, excluding the excited electron, first couple to a well defined LS term of definite total angular momentum J_c. Then, the excited Rydberg electron couples to this value of J_c to give a final value of $J = 7/2$, $5/2$, or $3/2$. According to the measurements of Ford *et al.* [41], the terms associated with the $3p^5 3d^5 4s^2$ configuration in order of increasing level energy are $^7P_4$, $^7P_3$, and $^7P_2$. Hence for resonance 14 we must couple $j = 1/2$ of the $4s$ electron to $J_c = 4$. We immediately see that the only possible value of J which satisfies the dipole selection rules is $J = 7/2$, i.e., only one state is allowed. Next we consider the case of resonance 15. Here we must couple $j = 1/2$ to $J_c = 3$. In this case, however, J can be coupled to J_c to give either $J = 7/2$ or $5/2$, both of which are allowed by the dipole selection rules. Hence, unlike resonance 14, resonance 15 can, in fact, be composed of two separate states. This also proves to be the case for resonance 17, which has $J_c = 2$. In this way we can qualitatively explain why resonances 15 and 17 should be composed of two states while resonance 14 should not.

The only other resonances which are clearly discernable in Fig. 2(h) are 19, 24, and 29. As in the case of the three largest resonances, these lines are split in energy by nearly the same amount as found for the fine-structure limits of the $3p^5 3d^5 4s^2(^7P)$ configuration. Hence we presume that these lines must then be associated with the $3p \rightarrow 6s$ Rydberg excitation. However, due to the relative weakness of these lines, we cannot make any assessment as to whether lines 24 and 29 are, in fact, split into two components, although at least line 24 appears to be broader than line 19.

The Rydberg excitations which characterize satellite 34 are somewhat similar to those of satellite 33, although the strongest lines, 16, 18, and 22+23, are weaker overall and they appear at higher photon energies than does the first Rydberg series of satellite 33. As in the case of satellite 33, however, their relative energy spacing is nearly the same as the fine-structure splitting of the $3p^5 3d^5 4s^2(^7P)$ state. For this reason, and because they appear at higher photon energies, we believe these lines are associated with $3p \rightarrow 4d$ Rydberg excitation. This is again in accord with Schmidt *et al.* [8] although they could not resolve any of the peaks seen here. Furthermore, according to theory [24] the $3p \rightarrow 4d$ excitation should precede the $3p \rightarrow 6s$ excitation as clearly indicated by our data. Because satellite 34 is dominated by $3p \rightarrow 4d$ transitions, the most probable configuration of this satellite, using the same arguments as in the case of satellite 33, is $3d^4(^5D)4s4d$ and not $3d^4 4p^2$.

A comparison of line 16 in the spectrum of satellite 34 with line 14 in the spectrum of satellite 33 indicates that line 16 is visibly broader. As in the previous instance, the width of this line is related to the different ways in which the $4d$ Rydberg electron can couple to J_c of the core electrons. Unlike the previous case, however, five different states can result from coupling j to $J_c = 4$, while six states can result from the coupling of j to $J_c = 3, 2$ because $j = 5/2$ or $3/2$ for the d electron. We see evidence for at least four different states associated with the $3p \rightarrow 4d$ excitation with states 16a,b appearing in the spectrum of satellite 34, and states 16c,d appearing in the spectrum of satellite 25+26. The appearance of resonance 16 in these satellite spectra is quite different from that in the $3d(^5D)$ main line, Fig. 2(c), where it appears as a window. According to recent calculations by Dolmatov [30], the window profile of this resonance in the $3d(^5D)$ channel is a direct result of the interaction of this resonance with the $3p \rightarrow 3d$ resonance. Hence it is somewhat surprising that the shape of this resonance should be so different in these satellite spectra, especially since the $3p \rightarrow 3d$ excitation for these satellites appears nearly identical to that in the $3d(^5D)$ main line.

Excitation of the $3p$ electron to the next member of the d-Rydberg series is not nearly as pronounced as that of the $3p \rightarrow 6s$ orbital. To determine where the next member in the d-Rydberg series would lie, we performed a quantum-defect calculation using the series limits of Ford *et al.* [41] and the quantum-defect parameter δ determined from the experimental level energy of the $4d$ excited state. Of course, one cannot assume that the quantum-defect parameter for the lowest-lying member should be the same for the next highest member; however, this should at least give an estimate of where the next member should lie. Our calculation indicates that the $3p^5 3d^5 4s^2(^7P_4)5d$ state would overlap strongly with the $3p^5 3d^5 4s^2(^7P_2)4d$ state, which also explains, in part, the large width of this feature. Furthermore, using the energy spacing of the ^7P fine-structure splitting, we could then determine where the other branches of the excitation were located, i.e., for states with $J_c = 3$ and 2. This led us to assign lines 22, 27, and 31 as belonging to the $3p \rightarrow 5d$ Rydberg excitation. Because of the proximity of feature 30 to 31, and because of the possibility of the existence of various states corresponding to different fine-structure components, this line has also been assigned to the $3p \rightarrow 5d$ manifold. Another interesting aspect of satellite 34 is the clear appearance of resonances 14 and 15a. This suggests that there is a nontrivial amount of mixing between the various J states associated with $3p \rightarrow 5s$ excitation and $3p \rightarrow 4d$ excitation. This should not be surprising based on the results of earlier theoretical calculations [16,24]. As discussed previously, the only way theory could attain reasonable intensity for resonances 4–6 was to mix the J values for these states with those from the $3p^5 3d^6 4s^2(^6P)$ state.

The spectrum of satellite 25+26, Fig. 2(g), is markedly different from both satellites 33 and 34. No obvious Rydberg structure is apparent, although line 16 is clearly visible with some evidence of resonances 14 and 15, and a broad maximum unique to this spectrum dominates the Rydberg region. We can understand part of this on a qualitative level. Because this spectrum is a CIS recording of two unresolved lines, it will contain features of both, reflecting a simple superposition of the two independent CIS spectra. Examination of the assignments of these lines from Table I indicates that this unresolved satellite is a mixture of states which contain excited s, p, and d electrons. Hence it is not surprising that the CIS spectrum would appear so "strange." Due to the structure superposed on top of the broad maximum, it is likely composed of many smaller peaks with widths similar to

that of resonance 16. A more detailed understanding of the behavior shown here will require separation of this line into its constituent components before any CIS measurements are made. This may, in practice, require even better resolution than that shown in Fig. 1 so as to completely resolve line 25 from 26.

E. High-binding-energy satellites

At photon energies greater than 58 eV, additional satellites with binding energies greater than 35 eV become clearly visible. These satellites, designated by roman letters, are indicated in the PES spectrum of Fig. 7 recorded with a photon energy of approximately 90 eV. The upper portion of the figure shows the entire spectrum, while the lower portion focuses on the relatively weak satellite lines. These satellites seem to manifest themselves only at higher photon energies. Their relative strengths change little as a function of photon energy, remaining as shown in Fig. 7 from about 80 eV up to 120 eV. The relative intensities with respect to the $3d(^5D)$ main line of the four strongest of these satellites, A, D, E, and F, are shown as a function of photon energy in Fig. 8(a). Between 60 and 80 eV overlap between these satellites and the Coster-Kronig lines and other radiationless decays originating from the filling of the $3p$ hole make it difficult to make a precise determination of their behavior.

The relative intensities of the other primary photoionization satellites over the same photon energy range, namely, satellites 25 and 26, and 33 and 34 are shown in Figs. 8(c) and 8(b), respectively. As we determined the relative intensity of all lines in the data from a fit to multiple Pearson-7 functions, we were able to deduce the individual intensities of lines 25 and 26 even though we did not resolve them. In panels (b) and (c) we have also compared our results to previous PES measurements [15], the asterisks in the figure. We note that the designation of the line groups in Fig. 5 of this older work should be switched. As the previous measurements were not able to resolve satellite 25 from 26 and satellite 33 from 34, we have compared our sum of 25 and 26, and of 33 and 34 with the older PES measurements. In both cases, our summed results are indicated by the open circles in panels (b) and (c). The present results clearly indicate a systematically higher relative intensity for these satellites. The reason for this is relatively straightforward. As can be seen from Fig. 7, there is a non-negligible "foot" associated with the main $3d(^5D)$ photoionization line. This foot results primarily from unresolved satellites which lie very close in binding energy to the main line, see Fig. 1. We were able to remove the contribution of these satellites to the overall $3d(^5D)$ intensity by fitting the shape of the $3d(^5D)$ line with inclusion of these satellites. This procedure, however, was not done in the previous case. Hence the overall intensity of the $3d(^5D)$ line was, on average, found to be larger in the previous measurements, leading to smaller relative satellite intensities. We confirmed this by including the intensity of

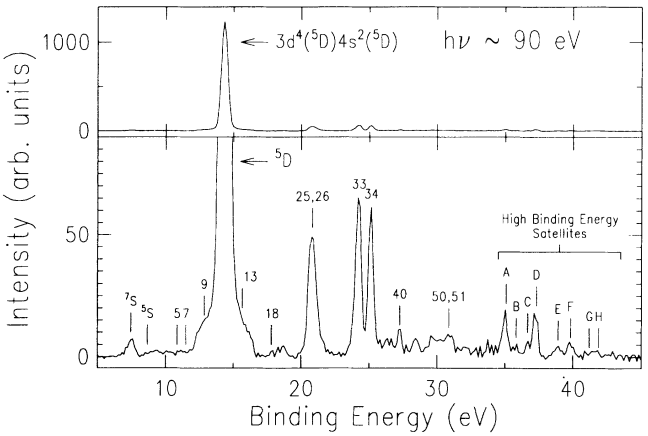

FIG. 7. PES spectrum recorded at the pseudomagic angle near $h\nu = 90.0$ eV. The upper portion shows the complete spectrum while the lower portion, an expansion of the upper part, focuses on the satellites. The high-binding-energy satellites which are not observed at lower photon energies are indicated by roman letters in the right hand portion of the spectrum.

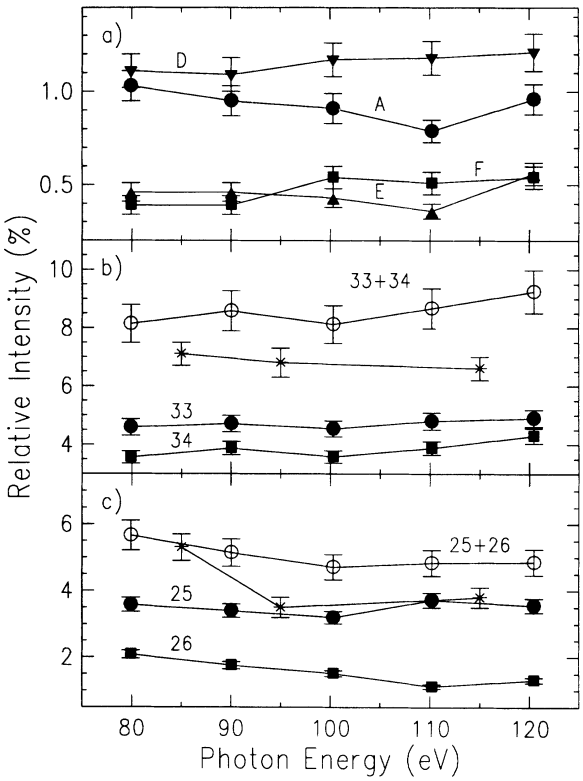

FIG. 8. Relative intensities, with respect to the $3d(^5D)$ main line, of major photoionization satellites and the most intense high-binding-energy satellites as a function of photon energy: (a) the high-binding-energy satellites A, D, E, and F; (b) satellites 33 and 34; and (c) satellites 25 and 26. Open circles in (b) and (c) are the sum of the satellite intensities displayed in each panel as discussed in the text. The asterisks are the earlier results of Ref. [15] for the satellite pairs. The lines connecting the data points are for guiding the eye only.

the adjacent satellites in the intensity of our main $3d(^5D)$ line, and reproduced the relative intensities of the older measurements within the experimental uncertainty. As pointed out in the earlier PES work, where measurements of these satellites were made up to 180 eV, the relative intensity of satellite 25+26 decreases slowly as a function of photon energy while that of line 33+34 increases gradually. Our summed results reflect the same behavior, even over this more limited photon energy range. For the high-binding-energy satellites analyzed here, the data suggest that these lines, except satellite A, may also be slowly increasing in relative intensity as a function of photon energy. However, to make this definitive, a much broader range of photon energies will need to be studied.

These high-binding-energy satellite lines have not been observed before, except for the two largest lines, A and D (see Fig. 2 of Ref. [14]), but no binding energies or discussion of their origin was given. In Table IV we list the binding energies of these satellites. As the optical data of Corliss and Sugar [39] only contain satellite designations for MnII up to the second ionization potential at 23.077 eV, they can be of no use in establishing the assignments of these satellites. However, we can take the following considerations into account to suggest a possible origin for these lines. First, since these lines lie far above the second ionization potential of Mn, they cannot be associated with configurations of the type $3p^6 3d^5 n\ell$. Another alternative are configurations of the type $3p^6 3d^4(^{2S+1}L)4s^2$ where the ^{2S+1}L term is other than the ^5D. To see what energy these non-^5D configurations would have, we performed single configuration Hartree-Fock calculations using the code of Froese Fischer [52]. Binding energies were obtained using the ΔSCF (self-consistent-field) method in which the total energy of the initial state is subtracted from the total energy of the final sate. The multiplets span an energy range of about 15 eV from the lowest-lying ^5D term at 13.463 eV to the highest-lying $^1S(1)$ term at 28.507 eV. The number in parentheses for the ^1S term refers to its seniority number. The values we calculated agree quite well with those calculated by Kobrin *et al.* [12] using a modified version of the Froese Fischer code. As can be clearly seen, even the highest binding energy for these states is too low to be a possible candidate for the high-binding-energy satellites. One could argue that an "excited" state of such a non-^5D configuration where a $4s$ electron is placed into a higher orbital could fall into the required binding energy range. However, as none of the "unexcited" non-^5D configurations are observed experimentally, it seems rather unlikely that such an "excited" state of a non-^5D configuration would be stronger than its "unexcited" counterpart.

TABLE IV. Binding energies of the high-binding-energy satellites.

Line	Binding energy (eV)
A	35.1(1)
B	35.8(1)
C	36.8(1)
D	37.4(1)
E	39.0(1)
F	38.9(1)
G	41.2(1)
H	41.9(1)

Another possibility is the configuration of the form $3p^6 3d^4 4p^2$. This particular configuration, but only allowing for the coupling of the $3d^4$ electrons to a ^5D term, was considered in Ref. [12] as a possible assignment for satellites 33 and 34. As pointed out in this reference, such a configuration can only result from configuration interaction in the initial state where the $3p^6 3d^5(^6S)4p^2(^6S)$ state mixes with the primary ground-state configuration. As discussed in Sec. III c, this mixing was found to be 5%. To get an estimate of the possible range of energies the various states of the $3p^6 3d^4 4p^2$ configuration could cover, we performed multiconfiguration Dirac-Fock ΔSCF calculations using the code of Grant *et al.* [53]. In order to reduce the total number of possible states which can result in the jj-coupling scheme, we restricted the total angular momentum of the four $4d$ electrons to be $J_c = 0$, as this value corresponds to that for the $^5D_0$ term. Furthermore, due to the jj-coupling rules for equivalent p electrons, only values equal to 0, 1, or 2 are possible, and hence the final value of the total angular momentum, J, can only be 0, 1, or 2. We note that these values of J are consistent with the dipole selection rules for photoionization of a d electron from the Mn ground state. With the above restrictions, we found that the states associated with this configuration range in binding energy from about 23.00 eV to nearly 41.00 eV. This energy range is already large enough to include most of the observed high-binding-energy satellites. Hence we believe that the $3p^6 3d^4 4p^2$ configuration, which results from initial-state configuration interaction, gives a very plausible explanation as to the origin of these lines. Of course, validation of this argument will have to await a comprehensive theoretical treatment of the problem.

IV. CONCLUSIONS

We have performed a high-resolution study of atomic Mn covering the $3p \rightarrow n\ell$ resonance region with special emphasis on the $3p \rightarrow 3d$ giant resonance. In a high-resolution PES spectrum we have observed nearly four times as many satellite lines as seen in past measurements. In particular, we have been able to identify, and characterize, many of the $4s$ and $3d$ satellite lines and, especially, the autoionizing-resonance states created by $3p \rightarrow n\ell$ excitations with a fair degree of confidence by correlating PES and CIS spectra on the basis of LS and sometimes intermediate-coupling schemes for both excitation and decay processes. The broad $3p \rightarrow 3d$ resonance around 50 eV was shown to contain a number of resonance states, some of which are likely to mix and others which do not. We have also determined the origin of the "dip" in the partial cross section of the $3d(^5D)$ main line. This feature probably results from the interaction of the primary $3p \rightarrow 3d(^6P)$ resonance with another nearby resonance which may originate from the $3p^5 3d^6 4p^2(^6P)$ excited-state configuration. Natural widths of most res-

onance states were determined by a fitting procedure, internally self-consistent with the entire CIS data set. The broadest resonance, the $3p \rightarrow 3d(^6P)$, was found to have a width of at most 1.5 eV, while most of the resonances arising from $3p \rightarrow n\ell$ ($n\ell \neq 3d$) excitations have a narrower width of about 0.1 eV. The first members of the $3p \rightarrow 5s, 6s, 4d, 5d$ series were identified and shown to primarily decay into excited Mn^+ channels, which are associated with satellite lines. This work led to a nearly complete partitioning, on a relative scale, of the photoionization cross section into its partial cross sections over the entire $3p$ resonance region. Conversely, the sum of our partial cross sections is in good agreement with the latest, most accurate photoabsorption measurements of Mn vapor.

In addition, we have studied the behavior of the main photoionization satellites as a function of photon energy from 80 to 120 eV at much higher resolution than in past experiments. This allowed us to separate previously unresolved lines so as to observe their individual behavior. And finally, we carried out a limited study of the photon energy dependence of some very high-binding-energy satellites, some of which have not been previously seen. We have discussed the possible origins of the previously unseen satellites and have concluded that they likely originate from initial-state configuration interaction of the $3p^6 3d^5 4p^2(^6S_{5/2})$ configuration with the primary $3p^6 3d^5 4s^2(^6S_{5/2})$ configuration. Various theoretical results are seen to reproduce the gross features of the resonance region in a semiquantitative way. However, detailed features such as the number and identity of resonance states, their widths and decay dynamics, and the mixing of the resonance configurations are predicted poorly or not at all. With the present data as a guide, it should be possible to develop an adequate theoretical model of the electronic structure and dynamics of this complex atom.

ACKNOWLEDGMENTS

S.B.W. would like to thank the Alexander von Humboldt foundation for support during the analysis of the experimental data and U. Becker for his hospitality at the FHI-MPG. M.O.K. is supported by the U.S. Department of Energy Basic Energy Sciences under Contract No. DE-AC05-850R21400 with Martin Marietta Energy Systems Inc., and C.D.C. by the National Science Foundation under Grant No. NSF-PHY-8907286, which also provided support for the experimental portion of this work. P.v.d.M. acknowledges support by the Oak Ridge National Laboratory and the Netherlands Organization for Scientific Research during the experiment. The Synchrotron Radiation Center, Stoughton, Wisconsin, is supported by the National Science Foundation under Grant No. DMR-9212658.

[1] J. P. Connerade, M. W. D. Mansfield, and M. A. P. Martin, Proc. R. Soc. London Ser. A **350**, 405 (1976).
[2] R. Bruhn, B. Sonntag, and H. W. Wolff, Phys. Lett. **69A**, 9 (1978).
[3] M. Meyer, Th. Prescher, E. von Raven, M. Richter, E. Schmidt, B. Sonntag, and H.-E. Wetzel, Z. Phys. D **2**, 347 (1986).
[4] J. W. Cooper, C. W. Clark, C. L. Cromer, T. B. Lucatorto, B. F. Sonntag, and F. S. Tomkins, Phys. Rev. A **35**, 3970 (1987).
[5] J. W. Cooper, C. W. Clark, C. L. Cromer, T. B. Lucatorto, B. F. Sonntag, E. T. Kennedy, and J. T. Costello, Phys. Rev. A **39**, 6074 (1989).
[6] J. T. Costello, E. T. Kennedy, B. F. Sonntag, and C. W. Clark, Phys. Rev. A **43**, 1441 (1991).
[7] R. Bruhn, E. Schmidt, H. Schröder, and B. Sonntag, Phys. Lett. **90A**, 41 (1982).
[8] E. Schmidt, H. Schröder, B. Sonntag, H. Voss, and H. E. Wetzel, J. Phys. B **18**, 79 (1985).
[9] B. Hermsmeier, C. S. Fadley, M. O. Krause, J. Jiménez-Mier, P. Gerard, and S. T. Manson, Phys. Rev. Lett. **61**, 2592 (1988).
[10] B. D. Hermsmeier, C. S. Fadley, B. Sinkovic, M. O. Krause, J. Jiménez-Mier, P. Gerard, T. A. Carlson, S. T. Manson, and S. K. Bhattacharya, Phys. Rev. B **48**, 12425 (1993).
[11] M. O. Krause, T. A. Carlson, and A. Fahlman, Phys. Rev. A **30**, 1316 (1984).
[12] P. H. Kobrin, U. Becker, C. M. Truesdale, D. W. Lindle, H. G. Kerkhoff, and D. A. Shirley, J. Electron Spectrosc. Relat. Phenom. **34**, 129 (1984).
[13] R. Malutzki, M. S. Banna, W. Braun, and V. Schmidt, J. Phys. B **18**, 1735 (1985).
[14] V. Schmidt, Comments At. Mol. Phys. **17**, 1 (1985).
[15] J. Jiménez-Mier, M. O. Krause, P. Gerard, B. Hermsmeier, and C. S. Fadley, Phys. Rev. A **40**, 3712 (1989).
[16] L. C. Davis and L. A. Feldkamp, Phys. Rev. A **17**, 2012 (1978).
[17] R. F. Reilman and S. T. Manson, Astrophys. J. Suppl. Ser. **40**, 815 (1979).
[18] M. Ya. Amusia, V. K. Dolmatov, and V. K. Ivanov, Zh. Eksp. Teor. Fiz. **85**, 115 (1983) [Sov. Phys. JETP **58**, 67 (1983)].
[19] L. J. Garvin, E. R. Brown, S. L. Carter, and H. P. Kelly, J. Phys. B **16**, L643 (1983).
[20] G. Doolen and D. A. Liberman, Phys. Scr. **36**, 77 (1987).
[21] E. B. Saloman, J. H. Hubbell, and J. H. Scofield, At. Data Nucl. Data Tables **88**, 1 (1988).
[22] V. K. Dolmatov, J. Phys. B **26**, L79 (1993).
[23] M. Ya. Amusia, V. K. Dolmatov, and V. K. Ivanov, J. Phys. B **16**, L753 (1983).
[24] L. J. Garvin, E. R. Brown, S. L. Carter, and H. P. Kelly, J. Phys. B **16**, L269 (1983).
[25] J. J. Yeh and I. Lindau, At. Data Nucl. Data Tables **32**, 1 (1985).
[26] M. Ya. Amusia, V. K. Dolmatov, and V. M. Romanenko, J. Phys. B **21**, L151 (1988).
[27] M. Ya. Amusia, V. K. Dolmatov, and M. M. Mansurov, J. Phys. B **23**, L491 (1990).

[28] V. K. Dolmatov, J. Phys. B **25**, L629 (1992).
[29] M. Ya. Amusia and V. K. Dolmatov, J. Phys. B **26**, 1425 (1990).
[30] V. K. Dolmatov, Phys. Lett. A **174**, 116 (1993).
[31] B. Sonntag and P. Zimmermann, Rep. Prog. Phys. **55**, 911 (1992), and references therein.
[32] M. O. Krause, T. A. Carlson, and A. Fahlman, Phys. Rev. A **24**, 1374 (1981).
[33] S. B. Whitfield, C. D. Caldwell, and M. O. Krause, Phys. Rev. A **43**, 2338 (1991).
[34] J. Jiménez-Mier, C. D. Caldwell, M. G. Flemming, S. B. Whitfield, and P. van der Meulen, Phys. Rev. A **48**, 442 (1993).
[35] R. P. Madden and K. Codling, Phys. Rev. Lett. **10**, 516 (1963).
[36] B. L. Henke, J. P. Knauer, and K. Premaratne, J. Appl. Phys. **52**, 1509 (1981).
[37] R. B. Cairns and J. A. R. Samson, J. Opt. Soc. Am. **56**, 1568 (1966)
[38] K. Pearson, Biometrika **16**, 157 (1924).
[39] C. Corliss and J. Sugar, J. Phys. Chem. Ref. Data **6**, 1253 (1977).
[40] C. Corliss and J. Sugar, J. Phys. Chem. Ref. Data **14**, 338 (1985).
[41] M. J. Ford, V. Pejcev, D. Smith, K. J. Ross, and M. Wilson, J. Phys. B **23**, 4247 (1990).
[42] B. W. Shore, J. Opt. Soc. Am. **57**, 881 (1967).
[43] U. Fano, Phys. Rev. **124**, 1866 (1961).
[44] D. W. Lindle, T. A. Ferret, U. Becker, P. H. Kobrin, C. M. Truesdale, H. G. Kerkhoff, and D. A. Shirley, Phys. Rev. A **31**, 714 (1985).
[45] P. van der Meulen, E. de Beer, C. A. de Lange, N. P. C. Westwood, and M. O. Krause, in *Synchrotron Radiation and Dynamic Phenomena*, Proceedings of the 48th International Meeting of Physical Chemistry, Grenoble, France, 9–13 September 1991, edited by Alberto Beswick, AIP Conf. Proc. No. 258 (AIP, New York, 1992), pp. 18–35.
[46] P. van der Meulen, M. O. Krause, C. D. Caldwell, S. B. Whitfield, and C. A. de Lange, Phys. Rev. A **46**, 2468 (1992).
[47] M. G. Flemming, J-Z. Wu, C. D. Caldwell, and M. O. Krause, Phys. Rev. A **44**, 1733 (1991).
[48] M. O. Krause, Franco Cerrina, Anders Fahlman, and T. A. Carlson, Phys. Rev. Lett. **51**, 2093 (1983).
[49] J. Jiménez-Mier, C. D. Caldwell, and M. O. Krause, Phys. Rev. A **39**, 95 (1989).
[50] F. Combet Farnoux, Phys. Rev. A **25**, 287 (1982).
[51] J. P. Connerade and A. M. Lane, Rep. Prog. Phys. **51**, 1439 (1988), and references therein.
[52] C. Froese Fischer, Comput. Phys. Commun. **14**, 145 (1978).
[53] I. P. Grant, B. J McKenzie, P. H. Norrington, D. F. Meyers, and N. C. Pyper, Comput. Phys. Commun. **21**, 207 (1980).